Available online at www.sciencedirect.com
SCIENCE DIRECT
Journal of Catalysis 232 (2005) 186–198
JOURNAL OF CATALYSIS
www.elsevier.com/locate/jcat

Novel microporous rhodium(II) carboxylate polymer complexes containing metalloporphyrin: syntheses and catalytic performances in hydrogenation of olefins

Tomohiko Sato, Wasuke Mori *, Chika Nozaki Kato, Emiko Yanaoka, Tomonori Kuribayashi, Ryoji Ohtera, Yuichi Shiraishi

Department of Chemistry, Faculty of Science, Kanagawa University, Hiratsuka, Kanagawa 259-1293, Japan

Received 15 December 2004; revised 2 February 2005; accepted 3 February 2005

Available online 12 April 2005

Abstract

Novel microporous rhodium(II) carboxylate polymer complexes containing metalloporphyrin, Rh_2[MTCPP] (M = H_2 **1**, Cu^{2+} **2**, Ni^{2+} **3**, Pd^{2+} **4**) (H_2TCPP = 4,4′,4″,4‴-(21*H*,23*H*-porphine-5,10,15,20-tetrayl)tetrakis benzoic acid), were synthesized and completely characterized by elemental analysis, TG/DTA, magnetic susceptibilities, FT-IR, DR-UV–vis, XRPD, BET analysis, and nitrogen adsorption measurements. These complexes possess carboxylate bridged dinuclear rhodium(II) sites and mononuclear copper(II), nickel(II), and palladium(II) centers in the porphyrin ring that form uniform micropores of ca. 5.0 Å. Furthermore, they show high surface areas and high nitrogen adsorption capacities and act as efficient heterogeneous catalysts for the hydrogenation of olefins at approximately 200 K. The unique bimetallic effects shown by metalloporphyrin and dinuclear rhodium sites in micropores were investigated by kinetic studies and hydrogen and propene adsorption–desorption measurements; the priority coordination of olefins onto metalloporphyrins and the intramolecular transfer of hydrogen from a rhodium center to a olefin molecule coordinated onto metalloporphyrin remarkably reflects the catalytic activities in hydrogenation.

Keywords: Rhodium carboxylate polymer complex; Metalloporphyrin; Microporous materials; Olefin hydrogenation; Adsorption property

1. Introduction

Development of an effective catalytic hydrogenation reaction to preferentially produce the desired materials has been a challenge from the viewpoint of both fundamental and industrial applications [1,2]. Rhodium-containing porous and nonporous materials have received attention as various heterogeneous, hydrogenation catalysts, such as organometallic Rh complexes on silica [3–7] or zeolite [8,9], diatomic Rh site on carbon [10], immobilization of Rh diphosphine complex on Al-MCM-41 [11], metal oxide deposits on Rh foil [12], molecular-imprinting Rh-dimer on silica surface [13–15], and polymer-attached Rh complex ($[Rh(NBD)LL]^+$ (L = polyphosphine ligand)) [16]. All of these materials are shown to be highly active in the hydrogenation of olefins, carbon dioxide, and carbon monoxide.

The synthesis of multimetallic active centers at the molecular level is one of the significant technologies utilized to develop more efficient hydrogenation catalysts [17–21]. Several supported multimetal catalysts have been extensively studied for their role in various heterogeneous reactions, and the roles of multimetallic centers have also been investigated. A few examples of rhodium-containing multimetal catalysts are as follows: $[Co_2Rh_2]\cdot(CO)_{12}/SiO_2$ for skeletal rearrangement of hydrocarbon [22]; Cu–M/NaY (M = Pt, Ir, Rh, Ru) [23], Ni–M/NaY (M = Ru, Rh, Pd, Pt) [24], and Pd–Rh/Al_2O_3 [25] for hydrogenation of the carbon–carbon multiple bond; $[H_2RhOs_3(CO)_{10}(acac)]$/

* Corresponding author. Fax: +81-463-58-9684.
E-mail address: wmori@kanagawa-u.ac.jp (W. Mori).

0021-9517/$ – see front matter
doi:10.1016/j.jcat.2005.02.007

Al_2O_3 [26], Rh–Fe/NaY [27], and M–Fe^{3+}/SiO_2 (M = Rh, Pt, Pd) [20] for CO hydrogenation; Ni–Rh/ZrO_2 [28] for CO_2 reforming; and Cu/Rh(100) catalysis for CO oxidation [29,30]. In some of the multimetallic catalysts, such as Ru–Pd/Al_2O_3 [31] and Pt on alkali-borosilicate [32], a hydrogen spillover behavior has been observed, which can accelerate the catalytic reactions significantly [33–35]. However, the studies on the heterogeneous catalytic activities involving a single active site of the multimetal catalysts are particularly challenging, given the inherent difficulties encountered in characterizing the active sites under the reaction conditions because of the difficulties in synthesizing the active and selective catalytic centers at molecular levels in heterogeneous catalysis [13–15].

The microporous inorganic–organic hybrid coordination polymers have attracted much attention because of their molecular adsorption [36–42], ion-exchange, and catalytic properties [36,39,43,45,46]. When compared with conventional porous materials such as zeolite or activated carbons, these coordination polymers are found to have potential for the future. This is due to the possibility of designing these coordination polymers to achieve a desirable pore shape and size, high porosity, and flexible framework, which are governed by the topological properties of the precursor metal ions and ligands. [Rh(diisocyanobiphenyl)$_2{}^+$Cl$^-$] is an example of a hydrogenation catalyst that uses inorganic–organic hybrid material [44]. Based on the efficient properties of porous inorganic–organic materials, we have specifically studied the syntheses and catalytic performances for the heterogeneous hydrogenation catalysis of rhodium carboxylate coordination polymers, such as rhodium(II) fumarate [Rh_2(*trans*-$OOCC_2H_2COO)_2]_n$ and rhodium(II) terephthalate [Rh_2(*p*-$OOCC_6H_4COO)_2]_n$. The uniform linear micropores in these complexes are constructed by the stacking or bonding of two-dimensional lattices of dinuclear transition metal carboxylates. Furthermore, single-site dinuclear transition metal centers in the uniform linear pores are significant characteristics for the use of these metal carboxylates as heterogeneous catalysts. In addition, all of the single metal centers can act as active centers during the heterogeneous catalysis. In addition, these complexes are capable of occluding large amounts of gases such as N_2, Ar, O_2, CH_4, and Xe and show the highest catalytic activities under the conditions of low temperature (255 K) and low pressure (30 Torr) during the hydrogenation of ethene, propene, and 1-butene [43,45]. Very recently, when tested among some rhodium-containing materials such as rhodium fumarate, rhodium terephthalate, and the other reported materials, the rhodium carboxylate polymer complex with a porphyrin ring, H_2TCPP (H_2TCPP = 4,4′,4″,4‴-(21*H*,23*H*-porphine-5,10,15,20-tetrayl)tetrakis benzoic acid), was demonstrated to exhibit the highest catalytic activity for the hydrogenation of propene at lower reaction temperatures (ca. 200 K) [43,46]. As these studies progressed, we focused chiefly on the syntheses of dinuclear rhodium(II) carboxylates with metalloporphyrin, MTCPP (M = Cu^{2+}, Ni^{2+}, and Pd^{2+}), as bimetal hydrogenation catalysts.

In this study, we have synthesized novel Rh_2[MTCPP] (M = H_2 **1**, Cu^{2+} **2**, Ni^{2+} **3**, Pd^{2+} **4**, as shown in Fig. 1) and completely characterized it by elemental analysis, FT-IR, DR-UV–vis, magnetic susceptibilities, BET surface area, pore size distribution, and nitrogen adsorption measurements. In this paper, we specifically report the catalytic performances of Rh_2[MTCPP] for the heterogeneous hydrogenation of ethene, propene, and 1-butene at low temperatures from 194 to 255 K, the unique bimetallic effects between metal centers of porphyrin rings, and the bridged dinuclear rhodium sites in uniform micropores.

2. Experimental

2.1. Materials

The following chemicals were used as received without further purification: $CuCl_2$, $NiCl_2 \cdot 6H_2O$, $PdCl_2$, NaOH, $CH_3COOC_2H_5$, HCl, *N*,*N*-dimethylformamide, and dehydrated methanol (quantitative analysis grade) (Wako). H_2TCPP was purchased from Tokyo Chemical Industries. Ethene, propene, 1-butene, and hydrogen (quantitative analysis grade) were purchased from the Takachiho Chemical Industrial Co., Ltd. Rh_2[H_2TCPP] (**1**) was synthesized and purified by a published method [43,46].

2.2. Instrumentation and methods

^{1}H-NMR spectra in DMSO-d_6 were recorded at 399.65 MHz with a JEOL JNM-EX400 FT-NMR spectrometer with a JEOL EX-400 NMR data-processing system. Chemical shifts, δ, were referenced to DMSO-h_6. The diffuse reflectance DR-UV–vis spectra were measured on a JASCO V-560 spectrophotometer equipped with a 60-mm integrating sphere, at a collection speed of 200 nm/min in the region of 200–800 nm. The samples were run without dilution, and Spectralon was used as a reference material. The spectra were displayed in $F(R)$ Kubelka–Munk units, where $F(R) = (1 - R)^2/2R = k/S$, and k and S are the absorption and scattering coefficients, respectively [61]. A JASCO FT/IR-300 spectrophotometer was used to measure the infrared (IR) spectra in the region of 4000–400 cm^{-1} with the use of nujol mull. The elemental analyses were carried out on a Perkin–Elmer PE 2400 II elemental analyzer installed at Kanagawa University. The elemental analysis of copper atoms was performed by gravimetric analysis. Thermogravimetric (TG) analysis and differential thermal analysis (DTA) were performed with a Rigaku TG8101D and TAS 300 data-processing system with an aluminum pan under air. The heating rate was 2 K/min, and α-Al_2O_3 was used as a reference material. The temperature dependence of the magnetic susceptibilities was measured with a Quantum Design MPMS-5S SQUID magnetometer in the temperature

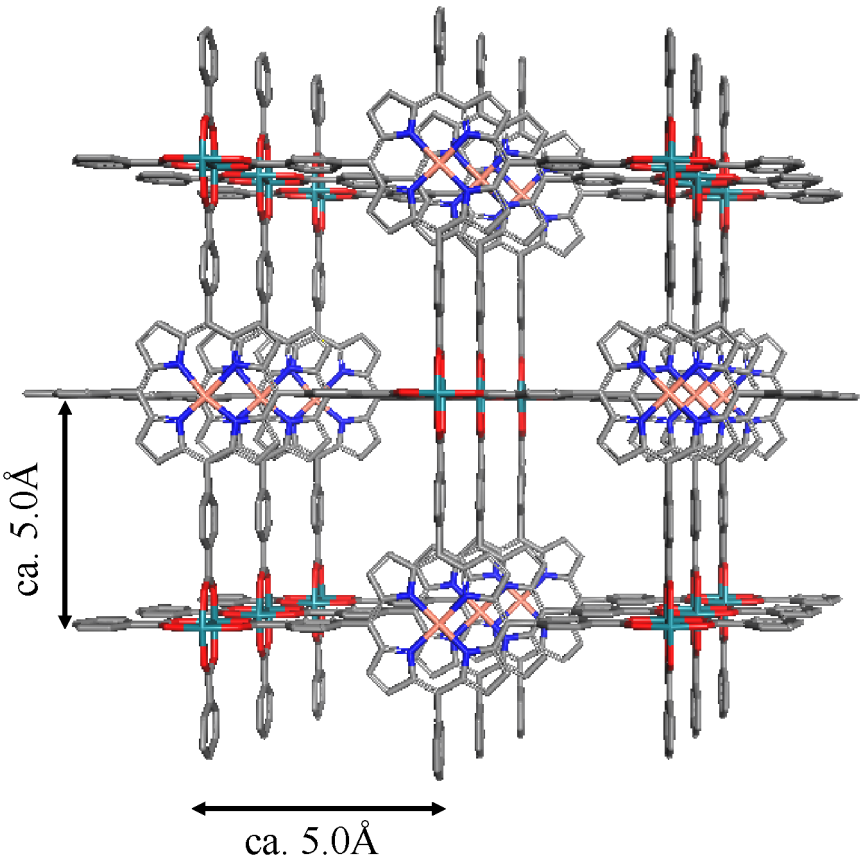

Fig. 1. Deduced molecular structure of Rh_2[MTCPP] (M = H_2 **1**, Cu^{2+} **2**, Ni^{2+} **3**, Pd^{2+} **4**). Elements are color-coded: rhodium (green), carbon (gray), nitrogen (blue), oxygen (red), and M (pink).

range of 2–300 K. The applied magnetic field was 1.0 T for complex **1** and 0.5 T for complex **2**–**4**. The susceptibilities were corrected for the diamagnetism estimated from Pascal's constants. The effective magnetic moments (μ_{eff}) were calculated from the equation $\mu_{\text{eff}} = 2.83(\chi_A T)^{1/2}$, where χ_A is the atomic magnetic susceptibilities. The X-ray powder diffraction (XRPD) data were collected with a Mac Science M18XHF^{22}-SRA target Cu diffractometer with Cu-K_α radiation ($\lambda = 0.15406$ nm, 35.0 kV, 200.0 mA). The temperature dependence of the amounts of occluded N_2 gas for all complexes was determined with the use of a Cahn 1000 electric balance at 20 Torr, where 1 Torr = (101325/760) Pa, in a temperature range of 77.5–200 K. Each sample was set in the apparatus, and the guest solvents present in the pore and at the surface were removed under vacuum. Nitrogen gas was dosed into the adsorption chamber, and the adsorption equilibrium was established; the change in the weight of the sample was measured subsequently. Adsorption isotherms were measured with a Micromeritics ASAP 2010 volumetric adsorption apparatus (Shimadzu Co. Ltd.). Before the adsorption measurements, the samples were degassed under vacuum at 273 K. The adsorption isotherms were measured in the relative pressure (P/P_0, where P_0 = saturation pressure) range between 10^{-5} and 1. The specific surface area was obtained from the Brunauer–Emmett–Teller (BET) equation [62]. The pore size distributions were obtained by the Horvath–Kawazoe (HK) method [63].

2.3. Synthesis of Cu^{2+}TCPP [48]

A mixture of $CuCl_2$ (68.0 mg, 0.506 mmol) and H_2TCPP (200 mg, 0.252 mmol) in DMF (100 cm^3) was refluxed at 433 K for 6 h. The mixture was centrifuged, washed with acetone, and then dried under vacuum at 373 K for 3 h. [Yield: 82.0%. Elemental anal. Found: C, 65.36; H, 3.49; N, 6.49; Cu, 7.29%. Calcd. for $C_{48}H_{31}N_4O_{9.5}Cu$ = $[Cu(C_{48}H_{28}N_4O_8)] \cdot 1.5H_2O$: C, 65.56; H, 3.55; N, 6.37; Cu, 7.23%. TG/DTA data: 3.4% weight loss below 546 K, suggesting the presence of 1.5 H_2O (3.1%).] The decomposition began approximately between 596 and 638 K, and an exothermic peak was obtained at 616 K. [Infrared spectrum (nujol mull, Table 1): 1696 (s) [$\nu_{C=O}$], 1606 (m), 1567 (w), 1512 (w), 1456 (m), 1425 (m), 1343 (m) [$\nu_{C=N}$], 1289 (m), 1176 (w), 1101 (w), 1002 (w) [δ_{C-H}], 795 (m), 715 (w), 460 (s) cm^{-1}. ^1H NMR spectrum (in DMSO-d_6, Fig. S1b): δ 13.19 [–COOH].] Because of the presence of paramagnetic metal ions in the center of the porphyrin ring, a broad band for Cu^{2+}TCPP was observed, and the peak corresponding to the N–H groups disappeared. The effective magnetic moment for Cu^{2+}TCPP was observed at 298 K (Figs. S2 and S3). [Found: μ_{eff} = 1.72 B.M. Calcd for $S = 1/2$:

Table 1
Selected IR spectral data (cm^{-1}) of complexes **1**–**4**

Complexes		–COOH	C–H rocking vibrations	$\nu_{asym}(CO_2)$	$\nu_{sym}(CO_2)$	$\Delta(\nu_{asym} - \nu_{sym})$
H_2TCPP		1696	1020, 985, 966	–[a]	–[a]	–
CuTCPP		1696	1001	–[a]	–[a]	–
NiTCPP		1691	1002	–[a]	–[a]	–
PdTCPP		1689	1012	–[a]	–[a]	–
$Rh_2[H_2TCPP]$	**1**	–[b]	1012, 966	1594	1459	135
$Rh_2[Cu^{2+}TCPP]$	**2**	–[b]	1001	1594	1461	133
$Rh_2[Ni^{2+}TCPP]$	**3**	–[b]	1002	1594	1461	133
$Rh_2[Pd^{2+}TCPP]$	**4**	–[b]	1012	1594	1461	133

[a] No separated peaks were observed due to the coordination of rhodium atom to the carboxylate groups of MTCPP.
[b] No peak was observed due to the starting materials MTCPP, showing the high purity of Rh_2[MTCPP].

1.73 B.M. DR-UV–vis spectra: 473 (sh) [Soret band], 541, 590 [Q-band] nm.]

2.4. Synthesis of Ni^{2+}TCPP [48]

A mixture of $NiCl_2 \cdot 6H_2O$ (180.8 mg, 0.761 mmol) and H_2TCPP (300 mg, 0.379 mmol) in DMF (150 cm^3) was refluxed at 433 K for 12 h. The mixture was filtered, washed with acetone, and then dried under vacuum at 298 K for 3 h. A reprecipitation was carried out with 200 ml of 3 M NaOH aqueous solution/400 ml of ethyl acetate. (At this point, porphyrin was present in the aqueous layer.) Approximately 1 M HCl was added until the intensely colored porphyrin was transferred into the organic layer. The organic layer was collected, washed with water, and filtered. The product was treated under vacuum at 373 K for 3 h to remove the solvents. [Yield: 82.0%. Elemental anal. Found: C, 65.48; H, 3.47; N, 6.27%. Calcd. for $C_{48}H_{32}N_4O_{10}Ni = [Ni(C_{48}H_{28}N_4O_8)] \cdot 2H_2O$: C, 65.26; H, 3.65; N, 6.34%. TG/DTA data: 4.1% weight loss below 573 K, suggesting the presence of 2 H_2O (4.1%).] The decomposition began approximately between 583 and 640 K, and an exothermic peak was obtained at 638 K. [Infrared spectrum (nujol mull, Table 1): 1691 (m) [$\nu_{C=O}$], 1606 (w), 1563 (w), 1461 (m), 1376 (m), 1350 (w) [$\nu_{C=N}$], 1288 (w), 1174 (w), 1097 (w), 1001 (w) [δ_{C-H}], 796 (w), 715 (w), 665 (w), 466 (s) cm^{-1}. ^{1}H NMR spectrum (in DMSO-d_6, Fig. S1c): δ 8.18, 8.20, 8.36, 8.38 (quartet) [Tolyl protons], δ 8.81 [β-pyrrole protons], δ 13.34 [–COOH].] No peak corresponding to the N–H groups was observed. [DR-UV–vis spectra: 451 [Soret band], 530, 575 [Q-band] nm.]

2.5. Synthesis of Pd^{2+}TCPP [47]

A mixture of $PdCl_2$ (53.8 mg, 0.304 mmol) and H_2TCPP (200 mg, 0.252 mmol) in DMF (100 cm^3) was refluxed at 433 K for 6 h. The mixture was centrifuged, washed with acetone, and dried under vacuum at 373 K for 3 h. [Yield: 70.0%. Elemental anal. Found: C, 60.17; H, 3.37; N, 6.52%. Calcd. for $C_{48}H_{35}N_4O_{11.5}Pd = [Pd(C_{48}H_{28}N_4O_8)] \cdot 3.5H_2O$: C, 60.16; H, 3.68; N, 5.85%. TG/DTA data: 6.3% weight loss below 559 K, suggesting the presence of 3.5 H_2O (6.6%).] The decomposition began approximately between 594 and 650 K, and an exothermic peak was obtained at 622 K. [Infrared spectrum (nujol mull, Table 1): 1689 (m) [$\nu_{C=O}$], 1605 (m), 1564 (w), 1460 (s), 1376 (m), 1351(w) [$\nu_{C=N}$], 1289 (m), 1176 (w), 1127 (w), 1102 (w), 1012 (m) [δ_{C-H}], 888 (w), 867 (w), 827 (w), 795 (m), 770 (w), 713 (w), 685 (w), 459 (s) cm^{-1}. ^{1}H NMR spectrum (in DMSO-d_6, Fig. S1d): δ 8.30, 8.32, 8.37, 8.39 (quartet) [Tolyl protons], δ 8.82 [β-pyrrole protons], δ 13.29 [–COOH].] No peak corresponding to N–H groups was observed. [DR-UV–vis spectra: 458 [Soret band], 524, 566, 662 [Q-band] nm.]

2.6. Synthesis of $Rh_2[Cu^{2+}TCPP]$ (2)

Complex **2** was synthesized by a modified, previously published method [43,46]. $Rh_2(CH_3COO)_4 \cdot 2H_2O$ (50 mg, 0.105 mmol) and Cu^{2+}TCPP (89.5 mg, 0.105 mmol) in MeOH (25 cm^3) were heated to 453 K at 5 K/min and autoclaved for 6 h. Subsequently, they were cooled to room temperature at a rate of 0.8 K/min. A dark brown precipitate was collected, washed with methanol, and dried at 373 K under vacuum for 6 h. [Yield: 94.9%. Elemental anal. Found: C, 52.48; H, 2.99; N, 4.68%. Calcd. for $C_{49}H_{32}N_4O_{11}CuRh_2 = [Rh_2(CuC_{48}H_{24}N_4O_8)] \cdot (CH_3OH) \cdot 2(H_2O)$: C, 52.45; H, 2.87; N, 4.99%. TG/DTA data: 6.1% weight loss below 424 K, suggesting the presence of CH_3OH and 2 H_2O (6.1%).] The decomposition began at approximately 573 K, and an exothermic peak was obtained at 613 K. [Infrared spectrum (nujol mull, Table 1): 1594 (m), 1558 (w), 1508 (w), 1462 (s), 1399 (m), 1376 (m), 1345 (w), 1275 (m), 1207 (w), 1178 (w), 1112 (w), 1000 (m), 870 (w), 846 (w), 827 (w), 800 (w), 769 (w), 722 (w), 466 (s) cm^{-1}. DR-UV–vis spectra: 465 [Soret band], 547, 590 [Q-band] nm. XRPD patterns: with relative intensities of 46.2, 34.3, 31.7, 28.2, 27.5, 100.0, and 39.9, respectively.]

2.7. Synthesis of $Rh_2[Ni^{2+}TCPP]$ (3)

Complex **3** was synthesized by the same method as that followed for complex **2**. $Rh_2(CH_3COO)_4 \cdot 2H_2O$ (35.5 mg, 0.072 mmol) and Ni^{2+}TCPP (63.0 mg, 0.074 mmol) were used as the starting materials. A dark brown precipitate was

obtained. [Yield: 94.6%. Elemental anal. Found: C, 52.31; H, 2.46; N, 4.90%. Calcd. for $C_{48.5}H_{32}N_4O_{11.5}NiRh_2$ = $[Rh_2(NiC_{48}H_{24}N_4O_8)] \cdot 0.5(CH_3OH) \cdot 3(H_2O)$: C, 52.26; H, 2.74; N, 5.08%. TG/DTA data: 3.2% weight loss below 428 K, suggesting the presence of 0.5 CH_3OH and 3 H_2O (6.3%).] The decomposition began at approximately 553 K, and an exothermic peak was obtained at 558 K. [Infrared spectrum (nujol mull, Table 1): 1594 (m), 1560 (w), 1461 (s), 1400 (m), 1376 (m), 1351 (m), 1276 (m), 1207 (w), 1176 (w), 1103 (w), 1004 (m), 865 (w), 844 (w), 827 (w), 796 (w), 767 (w), 719 (w), 468 (s) cm^{-1}. DR-UV–vis spectra: 453 [Soret band], 547, 590 (sh) [Q-band] nm. XRPD patterns: 2θ (°) = 9.05, 11.27, 16.00, 19.93, 40.99, and 47.61 with relative intensities of 95.4, 82.1, 64.0, 56.9, 100.0, and 49.6, respectively.]

2.8. Synthesis of $Rh_2[Pd^{2+}TCPP]$ (4)

Complex **4** was synthesized by the same method as that followed for complex **2**. $Rh_2(CH_3COO)_4 \cdot 2H_2O$ (50.0 mg, 0.105 mmol) and Pd^{2+}TCPP (94.0 mg, 0.105 mmol) were used as the starting materials. A dark brown precipitate was obtained. [Yield: 84.0%. Elemental anal. Found: C, 48.74; H, 3.26; N, 4.64%. Calcd. for $C_{49}H_{37}N_4O_{13.5}PdRh_2$ = $[Rh_2(PdC_{48}H_{24}N_4O_8)] \cdot (CH_3OH) \cdot 4.5(H_2O)$: C, 48.64; H, 3.08; N, 4.63%. TG/DTA data: 6.3% weight loss observed below 523 K, suggesting CH_3OH and 4.5 H_2O (9.3%).] Decomposition began at around 523 K with an exothermic peak at 570 K. [Infrared spectrum (nujol mull, Table 1): 1594 (m), 1551 (w), 1524 (w), 1460 (s), 1397 (m), 1376 (m), 1351 (m), 1275 (m), 1176 (w), 1102 (m), 1015 (m), 966 (w), 865 (w), 844 (w), 824 (w), 795 (w), 766 (w), 715 (w), 457 (s) cm^{-1}. DR-UV–vis spectra: 459 [Soret band], 525, 572 (sh), 658 [Q-band] nm. XRPD patterns: 2θ (°) = 7.99, 10.2, 11.19, 12.88, 21.52, 39.22, 40.96, and 47.70 with relative intensities of 56.4, 50.8, 40.8, 35.7, 32.6, 36.3, 100.0, and 38.5, respectively.]

2.9. Catalytic hydrogenation of olefins

The hydrogenation reactions of olefins (ethene, propene, and 1-butene) were carried out at 194, 220, and 255 K, respectively. Complexes **1**–**4** were placed in a reaction vessel, which was connected to a conventional closed gas circulation system (155.7 cm^3). After the evacuation was carried out at 298 K, the reaction gas, comprising 30 Torr olefin and 60 Torr H_2, was introduced. The hydrogenation products were determined by gas chromatography (GC). The reaction product was analyzed by GC (TCD, Porapak Q, and activated alumina stainless columns), and assignments were made by a comparison of these with the authentic samples analyzed under the same conditions.

3. Results and discussion

3.1. Synthesis and characterizations of complexes 1–4

Rh_2[MTCPP] (M = H_2 **1**, Cu^{2+} **2**, Ni^{2+} **3**, Pd^{2+} **4**) were synthesized by the ligand-exchange reaction of rhodium(II) acetate with MTCPP prepared from commercially available H_2TCPP and a metal chloride ($CuCl_2$, $NiCl_2 \cdot 6H_2O$, and $PdCl_2$), as shown in Scheme 1. The purity and composition of each of the starting MTCPP were obtained by elemental analysis, DR-UV–vis spectra, and ^{1}H NMR measurements (see Figs. S1–S3 for supporting information). The perfect insertion of metal atoms into the center of the porphyrin ring of **1** was impossible. The compositions and structures of complexes **1**–**4** were obtained by elemental analysis, infrared spectra, TG/DTA, ^{1}H-NMR, DR-UV–vis spectra, magnetic susceptibilities measurements, XRPD, adsorption isotherms, and pore size distributions.

For infrared spectra (Table 1) of MTCPP (M = H_2, Cu^{2+}, Ni^{2+}, and Pd^{2+}), the spectrum of H_2TCPP showed a triplet band at 1020, 985, and 966 cm^{-1} due to the well-resolved

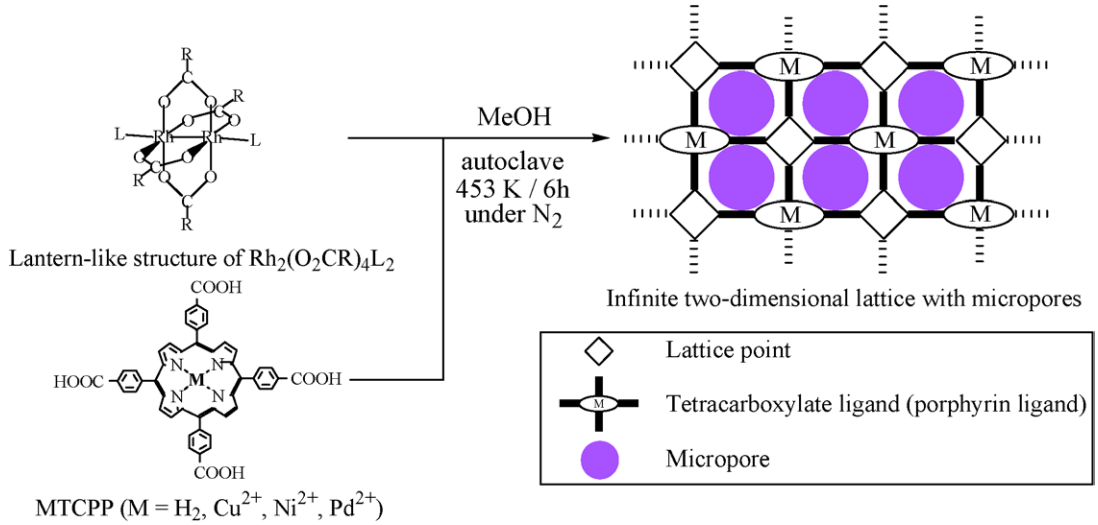

Scheme 1. Synthetic scheme for Rh_2[MTCPP] (M = H_2 **1**, Cu^{2+} **2**, Ni^{2+} **3**, Pd^{2+} **4**).

C–H rocking vibrations of the pyrrole ring, which shifted to 1001, 1002, and 1012 cm^{-1} as a singlet band, respectively, from the metallation at the center of the porphyrin ring for the formation of Cu^{2+}TCPP, Ni^{2+}TCPP, and Pd^{2+}TCPP [64,65]. For the MTCPP spectra, due to the –C=O stretching vibration in the –COOH group in MTCPP, the bands at 1696, 1696, 1691, and 1689 cm^{-1} separated into paired characteristic bands at (1594, 1459), (1594, 1461), (1594, 1461), and (1594, 1461), respectively, and due to the coordination of rhodium atom to the carboxylate groups of MTCPP, the adsorption bands for complexes **1**–**4** at 1594 cm^{-1} were assigned to the antisymmetric stretching vibrations of the carboxylate unit, and those at 1459, 1461, 1461, and 1461 cm^{-1} were assigned to the symmetric stretching vibrations [49]. The separations between $\nu_{asym}(CO_2)$ and $\nu_{sym}(CO_2)$ are 135, 133, 133, and 133 cm^{-1}. The separation width of two bands is characteristic of *syn–syn* bridging of the carboxylate groups of MTCPP [50].

To observe the structure of the bridging rhodium(II) sites in complexes **1**–**4**, the temperature dependencies of the magnetic susceptibilities for complexes **1**, **3**, and **4** (Fig. 2a) were simulated with the Bleaney–Bowers equation [51] for a $S = 1/2$ Heisenberg model of the dimer structure, as shown in Eq. (1), and that for complex **2** was simulated by Eq. (2):

$$\chi_A = \left(Ng^2\beta^2/kT\right)\left[1/3 + \exp(x)\right](1-\rho) + (3/4)\rho + N_\alpha, \quad (1)$$

$$\chi_A = \left(Ng_1^2\beta^2/kT\right)\left[1/3 + \exp(x)\right](1-\rho) + \left(Ng_2^2\beta^2/4kT\right) + (3/4)\rho + N_\alpha, \quad (2)$$

where $x = -2J/kT$, J is the exchange-coupling constant, ρ is the percentage of the monomer impurities, and N_α is the temperature-independent paramagnetism. The effective magnetic moments ($\mu_{eff} = 2.83(\chi_A T)^{1/2}$) versus temperature are shown in Fig. 2b and Table 2. In Fig. 2, the solid curves represent the theoretical dependence and the symbols represent the observed data. In the temperature range shown, the observed magnetic susceptibilities were in good agreement with the calculated magnetic susceptibilities, for constant values of g and J; the obtained parameters were $-2J = 1015$ cm^{-1}, $g = 1.98$, and $\rho = 1.3\%$ for complex **1**; $-2J = 938$ cm^{-1}, $g_1 = 2.00$, $g_2 = 1.95$, and $\rho = 0.05\%$ for complex **2**; $-2J = 883$ cm^{-1}, $g = 2.05$, and $\rho = 0.4\%$ for complex **3**; $-2J = 904$ cm^{-1}, $g = 2.01$, and $\rho = 2.2\%$ for complex **4**. The large magnetic moment of complex **2** (1.88 B.M.), due to paramagnetic copper(II) ion centered in the porphyrin ring, was consistent with the theoretical value (1.89 B.M.). The intradimer exchange integral J values for complexes **1**–**4** were similar to those of dinuclear rhodium(II) carboxylates such as dinuclear rhodium(II) acetate [52,53]. On the basis of the magnetic susceptibilities, the effective magnetic moments (μ_{eff}) were 0.82, 0.76, and 1.06 B.M. for complexes **1**, **3**, and **4** at 298 K, respectively. These values of μ_{eff} were smaller than that of 1.73 B.M./Rh^{2+} for the mononuclear rhodium atom with

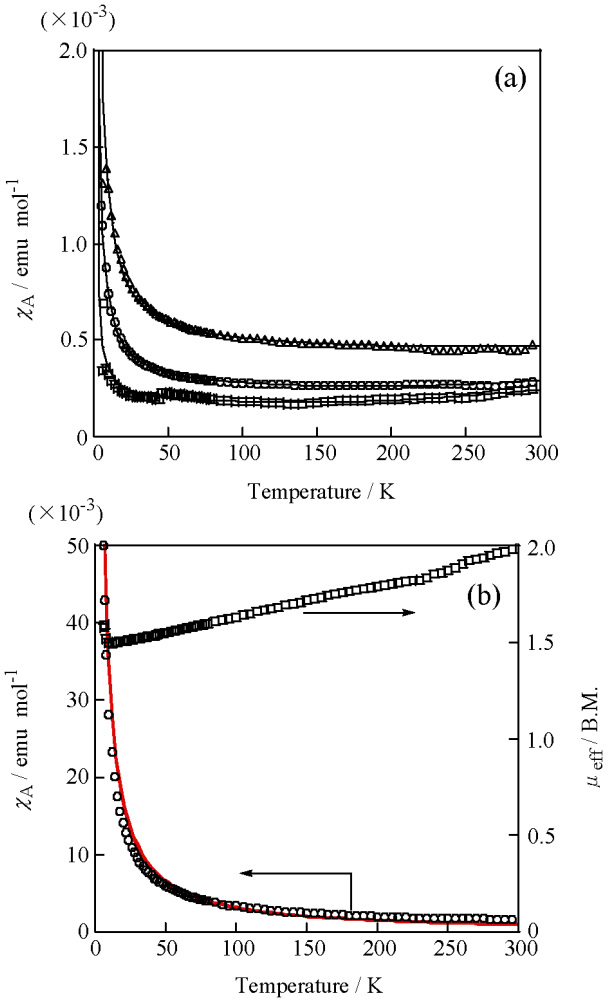

Fig. 2. (a) Temperature dependence of magnetic susceptibilities of Rh_2[MTCPP] [M = H_2 (**1**, ○), Ni^{2+} (**3**, □), and Pd^{2+} (**4**, △)]. (b) Temperature dependence of magnetic susceptibilities (○) and inverse of magnetic susceptibilities (●) of $Rh_2[Cu^{2+}TCPP]$ (**2**). The solid lines indicate the best fit curves calculated on the basis of the Bleaney–Bowers equation.

Table 2
Spin-exchange interactions J of Rh^{2+}–Rh^{2+} of complexes **1**–**4**

Complexes		g	$-2J$ (cm^{-1})	Monomer (%)	μ_{eff} (B.M.)	Equation
$Rh_2[H_2TCPP]$	**1**	1.9(8)	1015	1.3	0.82	(1)
$Rh_2[Cu^{2+}TCPP]$	**2**	2.0(0), 1.9(5)[a]	904	0.05	1.88	(2)
$Rh_2[Ni^{2+}TCPP]$	**3**	2.0(5)	883	0.4	0.76	(1)
$Rh_2[Pd^{2+}TCPP]$	**4**	2.0(1)	904	2.2	1.06	(1)

[a] g-value of paramagnetic copper(II) ion positioned in the porphyrin ring.

no magnetic interaction between Rh^{2+}–Rh^{2+}, showing the existence of antiferromagnetic interactions between the two carboxylate-bridged rhodium(II) ions.

The DR-UV–vis spectrum of **1** showed six main bands, including an intense Soret band (477 nm) and four characteristic visible absorption bands at 527, 567, 603, and 659 nm due to the presence of π–π^* and spin-forbidden transition bands in the porphyrin of previously described *para*-substituted *meso*-tetraphenylporphin derivatives [54]. These absorption bands were almost identical to those of the start-

Table 3
Microporosity obtained by Ar adsorption and maximum amount of adsorbed N_2 for complexes **1**–**4**

Complexes		Surface area[a]		Micropore volume (cm^3/g)	Pore size (Å)	Amount of adsorbed N_2 (mol/mol of Rh)
		BET	Langmuir			
$Rh_2[H_2TCPP]$	**1**	339 (168)	416 (206)	0.14	5.1	2.9 (5.7)[b]
$Rh_2[Cu^{2+}TCPP]$	**2**	373 (197)	456 (241)	0.16	5.1	3.2 (6.4)[b]
$Rh_2[Ni^{2+}TCPP]$	**3**	299 (157)	361 (190)	0.12	5.0	2.4 (4.7)[b]
$Rh_2[Pd^{2+}TCPP]$	**4**	318 (174)	387 (212)	0.13	5.0	2.5 (5.0)[b]

[a] [m^2/g ($\times 10^3$ m^2/mol of Rh)].
[b] mol/mol of porphyrin.

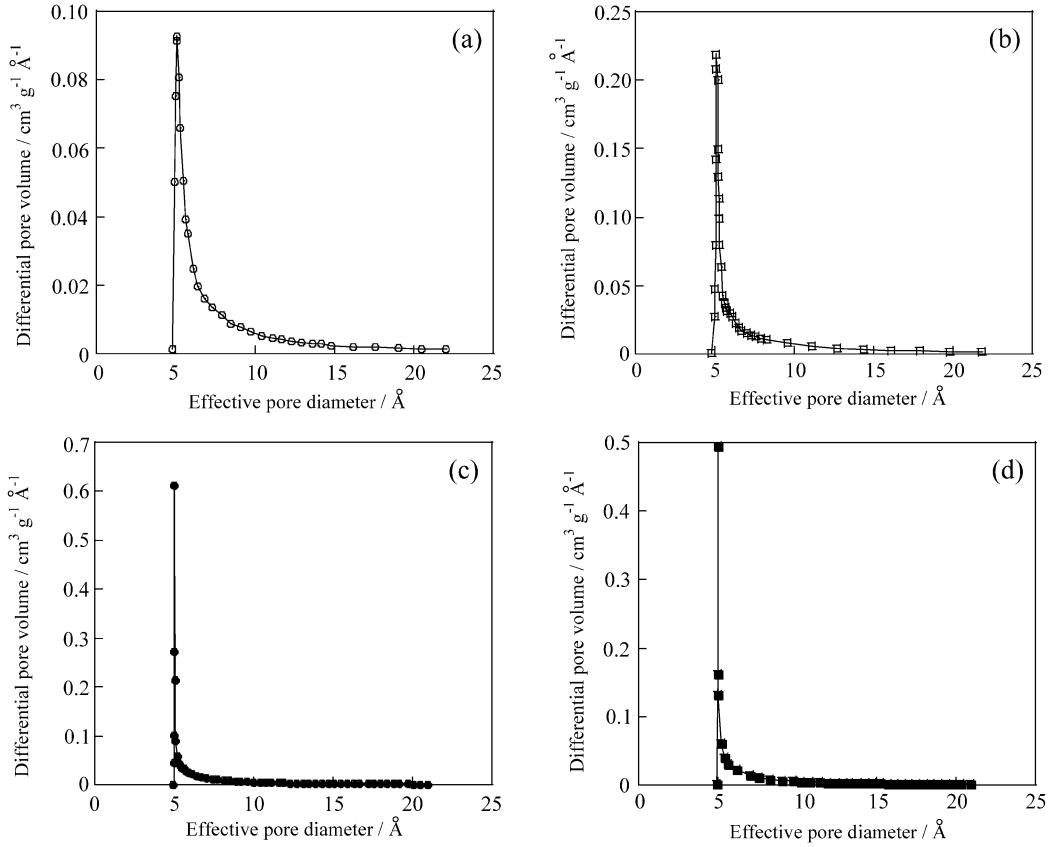

Fig. 3. Micropore size distributions for Rh_2[MTCPP], [M = (a) H_2 (○), (b) Cu^{2+} (□), (c) Ni^{2+} (●), (d) Pd^{2+} (■)].

ing material H_2TCPP, that is, 463 (Soret band) and 524, 562, 596, and 655 nm (Q-bands). The spectra of Cu^{2+}TCPP, Ni^{2+}TCPP, and Pd^{2+}TCPP showed three or four main bands at 466, 447, and 469 nm due to their Soret band at [547, 590], [534, 575], and [525, 572, 658] nm and their Q-bands, respectively. These absorption bands were different from those of H_2TCPP, showing that the metallation had occurred at the center of the porphyrin ring. With regard to DR-UV–vis spectra of complexes **1**–**4**, no change was observed due to the coordination of rhodium atoms to the carboxylate groups of MTCPP because the Rh–O band was hidden by the large Soret bands (from 430 to 480 nm) of MTCPP.

To examine the porosity of complexes **1**–**4**, high-resolution adsorption isotherms of argon at 87.3 K were measured under a relative pressure (P/P_0) range from 10^{-5} to 1. These adsorption isotherms of all complexes show typical isotherms of the Langmuir type, confirming the presence of micropores without mesopores. A sharp rise in argon adsorption at low relative pressures ($P/P_0 \leqslant 0.2$) indicated that the micropores were extremely uniform. Analyses of these isotherms yielded BET surface areas, micropore volumes, and effective pore size for all complexes shown in Table 3; the pore size distributions are shown in Fig. 3. In complexes **1** to **4**, one sharp peak was obtained at 5.1, 5.1, 5.0, and 5.0 Å, respectively, indicating that the obtained complexes have uniform micropores. The large surface areas (299 to 373 m^2/g) and the high micropore porosities (0.12 to 0.16 cm^3/g) in the area of inorganic–organic hybrid coordination polymers were due to the stacking of two-dimensional Rh_2[MTCPP] layers and other carboxylate coordination polymers [42]. XRPD data for complexes **1**–**4** also support this result.

Table 4
Catalytic activities for hydrogenation of propene catalyzed by complexes **1**–**4**[a]

Catalysts		TOF/g[b] [(TOF/Rh)][c]		
		At 194 K	At 220 K	At 255 K
$Rh_2[H_2TCPP]$	**1**	6.24×10^{-6} (3.10×10^{-3})	3.28×10^{-4} (0.16)	3.17×10^{-3} (1.57)
$Rh_2[Cu^{2+}TCPP]$	**2**	8.77×10^{-5} (4.62×10^{-2})	1.95×10^{-3} (1.03)	1.02×10^{-2} (5.39)
$Rh_2[Ni^{2+}TCPP]$	**3**	3.32×10^{-5} (1.74×10^{-2})	5.50×10^{-4} (0.29)	1.21×10^{-2} (6.36)
$Rh_2[Pd^{2+}TCPP]$	**4**	2.25×10^{-4} (1.24×10^{-1})	2.28×10^{-3} (1.25)	1.35×10^{-2} (7.38)

[a] Reaction conditions: catalyst, 10 mg; propene, 30 Torr; H_2, 60 Torr; and He, 1.4 Torr.
[b] TOF/g = [(mol of product)/(g s)] for hydrogenation of propene after 180, 15, and 5 min at reaction temperatures of 194, 220, and 255 K, respectively.
[c] TOF/Rh = [(mol of product)/((atom of Rh) s)] for hydrogenation of propene after 180, 15, and 5 min at reaction temperatures of 194, 220, and 255 K, respectively.

Table 5
Catalytic activities for hydrogenation of 1-butene catalyzed by complexes **1**–**4**[a]

Catalysts		TOF/g[b] [(TOF/Rh)][c]	
		At 220 K	At 255 K
$Rh_2[H_2TCPP]$	**1**	2.13×10^{-4} (0.11)	4.62×10^{-4} (0.23)
$Rh_2[Cu^{2+}TCPP]$	**2**	1.42×10^{-3} (0.75)	7.12×10^{-3} (3.54)
$Rh_2[Ni^{2+}TCPP]$	**3**	2.44×10^{-3} (1.28)	5.43×10^{-3} (2.70)
$Rh_2[Pd^{2+}TCPP]$	**4**	4.21×10^{-3} (2.31)	9.17×10^{-3} (4.57)

[a] Reaction conditions: catalyst, 10 mg; propene, 30 Torr; H_2, 60 Torr.
[b] TOF/g = [(mol of product)/(g s)] for hydrogenation of 1-butene after 15, and 5 min at reaction temperatures of 220 and 255 K, respectively.
[c] TOF/Rh = [(mol of product)/((atom of Rh) s)] for hydrogenation of 1-butene after 15, and 5 min at reaction temperatures of 220 and 255 K, respectively.

To observe the ability of complexes **1**–**4**, the adsorption isobars ($P = 20$ Torr) of nitrogen in the temperature range of 77.5 to 200 K were measured. Nitrogen was adsorbed into the complexes at temperatures below 200 K, and the amount of adsorbed gas finally attained the maximum around the boiling temperature of nitrogen. All of the complexes were capable of adsorbing a large amount of nitrogen, though amorphous H_2TCPP hardly adsorbed nitrogen (< 0.66 mole per mole of porphyrin). The maximum amounts of nitrogen adsorbed in complexes **1**–**4**, which were evaluated from the saturated amounts with isobars, were 2.9, 3.2, 2.4, and 2.5 mole per mole of rhodium(II) atoms, respectively, as summarized in Table 3. These absorbed amounts of nitrogen were approximately 2.1 to 3.7 times larger than those of rhodium(II) fumarate $[Rh_2(trans\text{-}OOCC_2H_2COO)_2]_n$ and rhodium(II) terephthalate $[Rh_2(p\text{-}OOCC_6H_4COO)_2]_n$ [42], and the order of maximum amount (**2** > **1** > **4** > **3**) was in good agreement with the order of the BET surface area.

3.2. Hydrogenation reactions of olefins catalyzed by complexes 1–4

The hydrogenation of olefin (ethene, propene, and 1-butene) catalyzed by complexes **1**–**4** was conducted at 194, 220, and 255 K, respectively. The results are summarized in Tables 4 and 5. The high activities of complexes **1**–**4** require reaction at a low temperature to secure a low initial rate. This also leads to freedom from complications arising from the influence of mass and heat transport. With regard to the hydrogenation of ethene, the reaction rates were extremely fast to observe, even at 194 K.

To obtain the time course of propene, hydrogenation at 194, 220, and 255 K (Figs. 4a–4c) and the high catalytic activities of complexes **1**–**4** were observed. Propane with 100% selectivity at all reaction temperatures was obtained as the product. At 194 K, an induction period less than 30 min was observed for complexes **1**–**4** because of the physisorption of the produced propane in the micropores. After 180 min, the conversions of complexes **1**–**4** attained 2.7, 47.1, 14.5, and 100%, respectively, showing that complex **4** was the most active, and their turnover frequencies (TOF = [(mol of product)/(g s)]) were 6.24×10^{-6}, 8.77×10^{-5}, 3.32×10^{-5}, and 2.25×10^{-4}, respectively, showing that the TOF of **4** was 2.6–36 times higher than those of complexes **1**–**3**; and the order of the activity of these complexes for propene hydrogenation was $Pd^{2+} > Cu^{2+} > Ni^{2+} \gg H_2$. At 220 K, the TOFs [(mol of product)/(g s)] of complexes **1**–**4** were, respectively, 3.28×10^{-4}, 1.95×10^{-3}, 5.50×10^{-4}, and 2.28×10^{-3} after 15 min. At 255 K, the conversions of all catalysts attained 100% within 30 min. In particular, the reaction catalyzed by **4** finished within 5 min. The TOFs [(mol of product)/(g s)] of **1**–**4** were, respectively, 3.17×10^{-3}, 1.02×10^{-2}, 1.21×10^{-2}, and 1.35×10^{-2} after 5 min. The catalytic results at 220 and 255 K also showed that complex **4** was the most active complex, and the order of the activity was the same ($Pd^{2+} > Cu^{2+} > Ni^{2+} > H_2$). In addition, these bimetallic effects of Cu–Rh, Ni–Rh, and Pd–Rh were not dependent on the BET surface area; rather they were dependent on the type of metal atoms centered in the porphyrin ring, as shown in Fig. 5. The 100% conversion after 5 min at 255 K and a TOF of 1.35×10^{-2} [(mol of product)/(g s)] (= 7.38 [(mol of product)/((atom of Rh) s)]) were observed for **4** and compared with those reported for other rhodium(II)-containing systems; the conversion of propene hydrogenation over $[Rh(NBD)(PolyPPh_2)_2]ClO_4$ [16] at 361 K could not exceed 50%, even after 7200 min. The TOF values of 9.80×10^{-4} [(mol of product)/(atom of Rh)] for $Cp_2Ta(CH_2)_2Rh(CO)_2$ observed at 318 K and 1.85×10^{-3} [(mol of product)/(atom of Rh)] for $Cp_2Ta(CH_2)_2Rh(CO)(PPh_3)$ observed at 318 K [10] were much lower (1×10^{-4} times) lower than that of **4**.

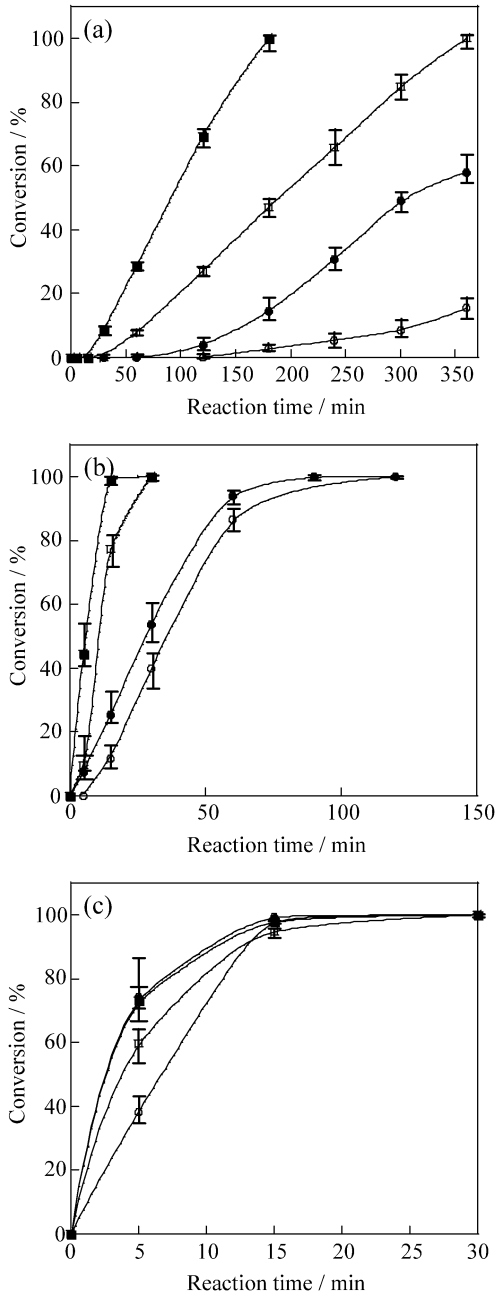

Fig. 4. Time course for hydrogenation of propene catalyzed by Rh_2[MTCPP] M = H_2 (○), Cu^{2+} (□), Ni^{2+} (●), Pd^{2+} (■) at (a) 194, (b) 220, and (c) 255 K. Reaction conditions: catalyst, 5 and 10 mg; propene, 30 Torr; H_2, 60 Torr.

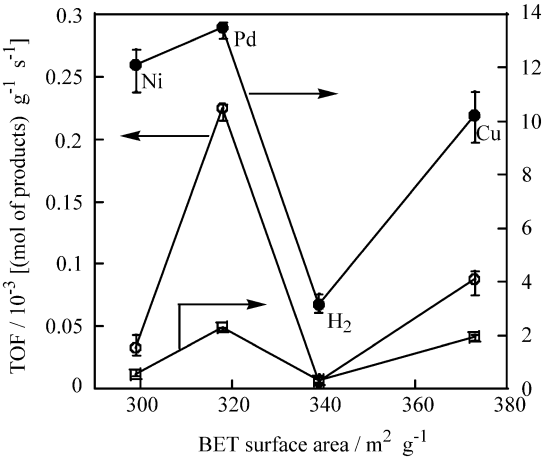

Fig. 5. Surface area dependence of TOFs for propene hydrogenation catalyzed by Rh_2[MTCPP] (M = H_2 **1**, Cu^{2+} **2**, Ni^{2+} **3**, Pd^{2+} **4**) at 194 (○), 220 (□), and 255 K (●).

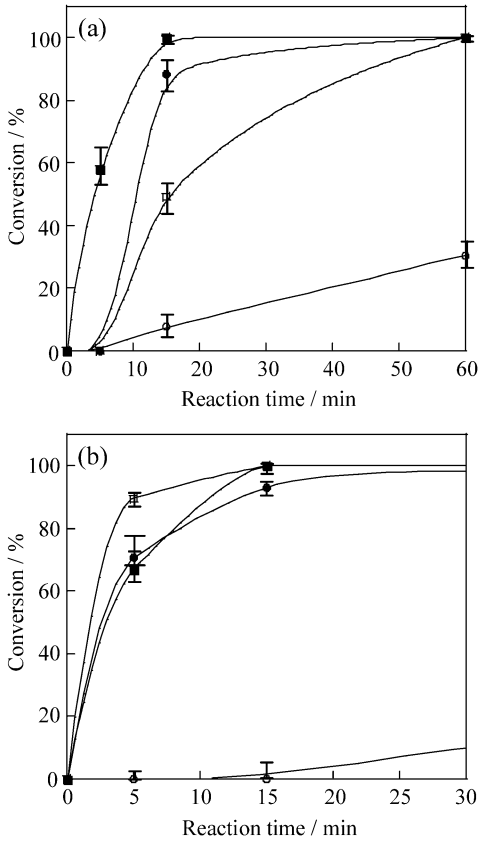

Fig. 6. Time course for hydrogenation of 1-butene catalyzed by Rh_2[MTCPP] M = H_2 (○), Cu^{2+} (□), Ni^{2+} (●), Pd^{2+} (■) (a) at 220 and (b) 255 K. Reaction conditions: catalyst, 10 mg; propene, 30 Torr; H_2, 60 Torr.

Metal-supported catalysts such as Pt/SiO_2 (0.37 mol/atom of Pt at 220 K) and Pd/SiO_2 (1.6 mol/atom of Pd at 201 K) [55] showed activities similar to that of **4**, but they required a higher reaction pressure (7.6×10^2 Torr).

Complexes **1**–**4** were also observed to catalyze the hydrogenation of 1-butene to butane (100% selectivity) at 220 and 255 K, as shown in Fig. 6 and Table 5. At 194 K, measurements were not reproducible because of the solidification of 1-butene. At 220 K, an induction period was observed for these complexes because of the physisorption of the produced butane. The conversions of complexes **1**–**4** attained 100% within 60 min. The TOFs [(mol of product)/(g s)] of **1**–**4** were 2.13×10^{-4}, 1.42×10^{-3}, 2.44×10^{-3}, and 4.21×10^{-3}, respectively, suggesting that complex **4** was the most active, and the order of the activity of these complexes for 1-butene hydrogenation at 220 K was $Pd^{2+} > Cu^{2+} \approx$

$Ni^{2+} \gg H_2$. At 255 K, the conversion attained 100% within 30 min. The highest TOF of complex **4** was 9.17×10^{-3}; the TOF was 19.8, 1.3, and 1.7 times those of complexes **1**–**3**; and the same order of activity ($Pd^{2+} > Cu^{2+} > Ni^{2+} > H_2$) was observed for these complexes for the hydrogenation of 1-butene. The observed TOF compares favorably with those reported for other heterogeneous systems involving supported metals. For example, $Cp_2Ta(CH_2)_2Rh(CO)_2$, with a TOF of 1.39×10^{-4} [(mol of product)/(atom of Rh)], has been reported to catalyze the hydrogenation of 1-butene. This TOF was much lower than that of **4**, 9.17×10^{-3} [(mol of product)/(atom of Rh)], at 255 K. In addition, the TOFs for this reaction have been reported for metal-supported catalysts such as Pt/Al_2O_3 (0.85 wt%) at 300 K (TOF: 12) (20 MPa) [55] and $Rh(C_5H_7O_2)_3/\gamma\text{-}Al_2O_3$ (0.23 wt%) at 300 K (TOF: 23.1) (20 MPa) [56], which had activities higher than that of complex **4**; however, they required conditions of high temperature (300 K) and high pressure (2.6×10^2 Torr).

As control experiments, the 1:1 (mol/mol) mixtures of $Rh_2(CH_3COO)_4 \cdot 2H_2O$ and MTCPP were used as catalysts for the hydrogenation of propene at 194 K, as shown in Fig. 7. No reaction was observed for any of the catalysts used. Despite the remarkable bimetallic effects observed for the hydrogenation catalysis mentioned above, the 1:1 (mol/mol) mixtures of $Rh_2[H_2TCPP]$ and MTCPP (M = Cu^{2+}, Ni^{2+}, and Pd^{2+}) also showed (1×10^{-1} times) activities lower than those of complexes **2**–**4** for the hydrogenation of propene at 194 K, as shown in Fig. 7. In addition, no nonporous rhodium carboxylate polymer complex showed any reaction for the hydrogenation reaction of propene at 194 K. These results indicate that (1) the hydrogenation reactions requires Rh centers, (2) the intramolecular distances between the metal atoms centered in the porphyrin ring and the Rh centers are critical for the hydrogenation reactions, and (3) the hydrogenation reaction occurs in the micropores.

3.3. Reaction mechanism including bimetallic effects of Rh^{2+}–Cu^{2+}, Rh^{2+}–Ni^{2+}, and Rh^{2+}–Pd^{2+} combinations

To understand the reaction mechanism including the bimetallic effect, the individual roles of the metal atoms centered in the porphyrin ring and the bridged dinuclear rhodium sites for the hydrogenation reactions were investigated. With regard to the hydrogenation reaction of olefins over rhodium-containing catalysts, the well-known hydrogenation mechanism involves four steps [57–60]: dissociation of hydrogen molecules located at the metal center to form hydrides, coordination of an olefin C=C double bond to the metal center, insertion into the Rh–H bond to form a half-hydrogenated alkyl species, and reaction of the alkyl with the remaining hydride. Based on our previous report regarding the H–D exchange reactions over microporous rhodium(II) fumarate and rhodium(II) terephthalate [43,45], these typical steps involved in the hydrogenation reaction occurred between the two-dimensional $[Rh_2(trans\text{-}OOCC_2H_2COO)_2]_n$ layers and $[Rh_2(p\text{-}OOCC_6H_4COO)_2]_n$ layers. With regard to the reaction mechanism of complexes **1**–**4**, the kinetic parameters, activation energies (E_a), activation enthalpies ($\Delta^{\ddagger}H$), and activation entropies ($\Delta^{\ddagger}S$) (Table 6), calculated on the basis of the reaction rates for hydrogenation reactions of propene catalyzed by rhodium(II) fumarate and complexes **1**–**4** in the temperature range of 194–255 K, also provided efficient aspects for the consideration of the reaction mechanism; the activation energies for

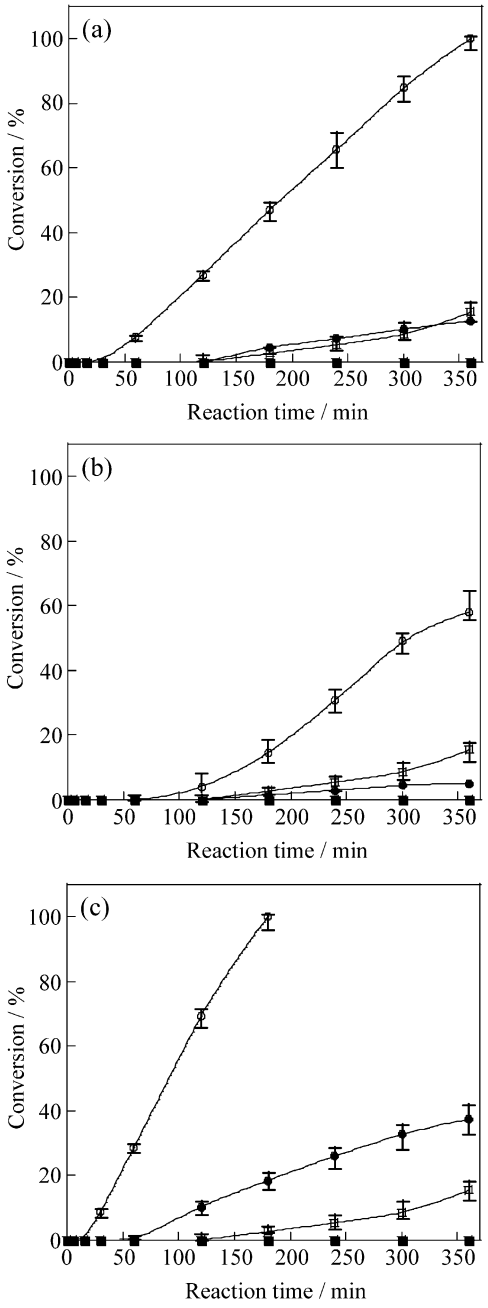

Fig. 7. Time course for hydrogenation of propene at 194 K catalyzed by $Rh_2[MTCPP]$ (○), $Rh_2[H_2TCPP]$ (□), the mixture of $Rh_2[H_2TCPP]$ + MCl_2 (●), and the mixture of $Rh_2(CH_3COO)_4 \cdot 2H_2O$ + MTCPP (■). M = (a) Cu^{2+}; (b) Ni^{2+}; (c) Pd^{2+}. Reaction conditions: catalyst, 10 mg; propene, 30 Torr; H_2, 60 Torr.

Table 6
Activation energies (E_a), activation enthalpies ($\Delta^{\ddagger}H$), and activation entropies ($\Delta^{\ddagger}S$) for the catalytic hydrogenation of propene at 255 K

Catalysts		Kinetic parameters		
		E_a (kJ/mol)	$\Delta^{\ddagger}H$ (kJ/mol)	$\Delta^{\ddagger}S$ (J/(K mol))
Rh fumarate		41.6	39.5	−518
$Rh_2[H_2TCPP]$	**1**	42.0	39.9	−517
$Rh_2[Cu^{2+}TCPP]$	**2**	32.0	29.9	−556
$Rh_2[Ni^{2+}TCPP]$	**3**	39.8	37.7	−525
$Rh_2[Pd^{2+}TCPP]$	**4**	27.6	25.4	−573

complexes **1**–**4** were 42.0, 32.0, 39.8, and 27.6 kJ/mol, respectively. The E_a value of complex **1** was similar to that of rhodium fumarate (41.6 kJ/mol), suggesting that the reaction mechanism at the rhodium center of **1** was the same as that of rhodium fumarate. In addition, the E_a values decreased in the order of **1** > **3** > **2** > **4** with the catalytic activities decreasing in the order of **4** > **2** > **3** > **1** for the hydrogenation of propene and 1-butene, suggesting that the metal atoms centered in the porphyrin ring remarkably influenced the activations of hydrogen molecules and/or olefin molecules. Furthermore, the activation entropies for rhodium fumarate and complexes **1**–**4** were −518, −517, −556, −525, and −573 J/(K mol), respectively, which were significantly smaller than that of Rh dimer-imprinted SiO_2 (−276 to −170 J/(K mol)) [13–15], suggesting that the conformation of the coordinated propene was highly regulated by the micropore walls of rhodium fumarate and complexes **1**–**4**.

Furthermore, to investigate the roles of Cu^{2+}, Ni^{2+}, and Pd^{2+} atoms centered in the porphyrin ring, the hydrogen and propene absorption–desorption measurements were performed at 77.4 and 273.2 K, respectively, as shown in Fig. 8. The saturated amounts of the adsorbed hydrogen at ca. 720 mmHg for complexes **1**–**4** were 76.3, 74.2, 59.6, and 57.4 cm^3 STP/g, respectively. In the desorption curves of hydrogen, the amounts of hydrogen desorbed were approximately the same as those of adsorbed hydrogen, indicating that very fast, reversible adsorption–desorption of hydrogen occurred in all of the complexes. Slight differences were observed for the adsorption–desorption behaviors among complexes **1**–**4**, suggesting that the activation of hydrogen was not influenced by the metal atoms centered in the porphyrin ring. The activation of the hydrogen molecule at the bridged rhodium centers was much faster than that of the reported Rh_2 centers at the SiO_2 surface, on which the presence of rhodium hydride species could be detected even at room temperature [13–15]. The result suggests that the hydride species could not be detected by magnetic susceptibility measurements after pretreatment under a hydrogen atmosphere of 20 Torr at 25 °C for 3 h. The unstable rhodium hydride species were formed at the rhodium centers of complexes **1**–**4**.

In contrast, the saturated amounts of adsorbed propene at ca. 650 mmHg were 59.3, 70.8, 40.3, and 54.8 cm^3 STP/g, respectively. Hystereses were observed in all of the desorption curves of propene. These desorption curves were different from the adsorption curves, showing that the physisorption of olefin molecules in micropores of complexes **1**–**4** was much stronger than that of hydrogen. The ratios of the residual amounts of propene molecules after desorption to the saturated amounts of adsorbed propene molecules at ca. 40 mmHg were 17.6, 16.0, 28.5, and 14.3, respectively, and the residual amounts were decreased in the order **4** < **2** < **3**, which was consistent with the reverse order of catalytic activities as mentioned above. Thus, a smooth reversibility of adsorption–desorption of olefin molecules led to higher catalytic activities for the hydrogenation reaction. These results suggest that the metal atoms centered in the porphyrin ring significantly reflect the coordination of the olefin molecules.

Finally, we proposed the reaction mechanism for Rh_2[MTCPP]. In the reactions of $Rh_2[H_2TCPP]$, the first step included both the addition of hydrogen to the rhodium center to form hydrides and the coordination of olefins. With regard to complexes **2**–**4**, the priority coordination of olefin onto the metal center of the porphyrin ring also occurred. At the dinuclear rhodium sites, insertion to the Rh–H bond to form a half-hydrogenated alkyl species and the reaction of an alkyl with a hydride occurred continuously. At the Cu^{2+}, Ni^{2+}, and Pd^{2+} centers of the porphyrin ring, the hydride species at the rhodium center were transferred to the coordinated olefin located in the center of the porphyrin ring to form alkyl species, and then the alkyl species reacted with a hydride species activated at the rhodium center to form the alkane. This intramolecular hydrogen transfer might significantly influence catalytic activities during hydrogenation. To our knowledge, this hydrogen transfer was the first example of catalytic behavior observed with inorganic–organic hybrid materials, though such a hydrogen transfer (hydrogen spillover) has already been observed in multimetallic oxides and multimetallic clusters [31–35].

4. Conclusion

Novel microporous rhodium(II) carboxylate polymer complexes with metalloporphyrin, Rh_2[MTCPP] (M = H_2 **1**, Cu^{2+} **2**, Ni^{2+} **3**, Pd^{2+} **4**) (H_2TCPP = 4,4′,4″,4‴-(21*H*,23*H*-porphine-5,10,15,20-tetrayl)tetrakis benzoic acid), were synthesized by ligand exchange reactions of rhodium acetate with MTCPP. These were completely characterized by elemental analysis, TG/DTA, magnetic susceptibility, FT-IR, DR-UV–vis, X-ray powder diffraction (XRPD), BET analysis, pore size distribution, and nitrogen adsorption measurements. These characterization results showed that (1) the carboxylate bridged dinuclear rhodium structure formed with mononuclear copper, nickel, and palladium located at the center of the porphyrin ring was formed in complexes **2**–**4**, and (2) the Rh_2[MTCPP] possessed numerous uniform micropores (ca. 5.0 Å in diameter) created by stacking of a two-dimensional lattice structures

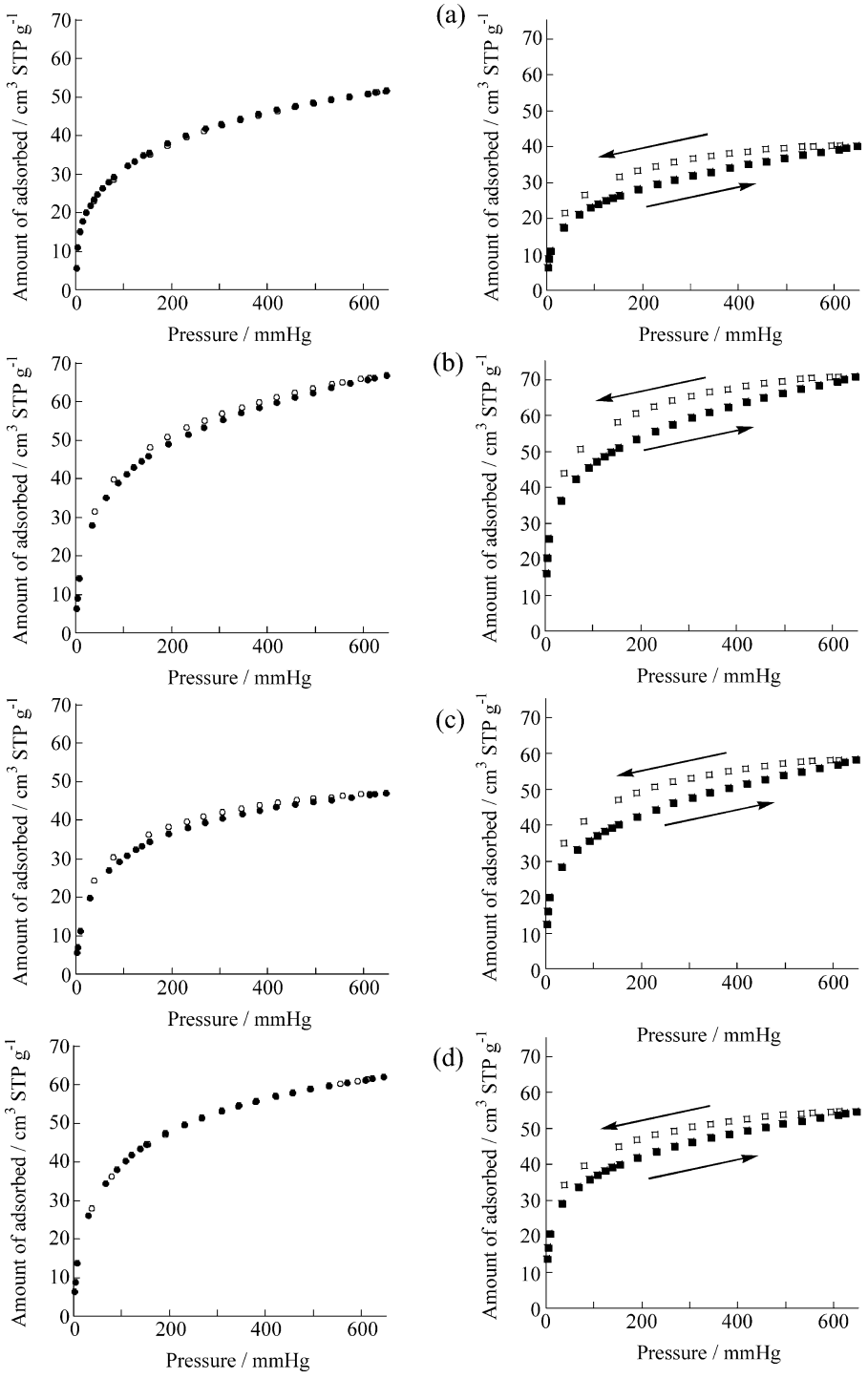

Fig. 8. Adsorption (black)–desorption (white) isotherms of hydrogen at 77.4 K (circle) and propene at 273.2 K (square) for Rh_2[MTCPP] (M = (a) H_2, (b) Cu^{2+}, (c) Ni^{2+}, (d) Pd^{2+}).

and possessed a high nitrogen adsorption capacity. With regard to the hydrogenation of ethene, propene, and 1-butene, (1) complexes **1**–**4** showed high turnover frequencies, and among these and the other reported rhodium-containing materials, it was the most active in complex **4**; (2) hydrogenation reactions occurred inside the micropores of complexes **1**–**4**; (3) the activation of the hydrogen molecule from Rh–H species occurred only at the dinuclear rhodium sites, and the metal centers of the porphyrin ring significantly influenced the coordination of olefins; and (4) the activated hydrogen at the bridged dinuclear rhodium sites was transferred from the coordinated olefin molecule to the metal center of the porphyrin ring. Catalytic reactions using microporous inorganic–organic hybrid materials, as demonstrated in this paper, could be used to create a new strategy for the development of more efficient catalysts.

Acknowledgments

We acknowledge Prof. S. Naito (Kanagawa University) for his advice on the catalytic reactions. This work was supported by a Grant-in-Aid for Specially Promoted Research (no. 15350088) from the Ministry of Education, Science, Sports and Culture of Japan. This work was also supported by a High-tech Research Center Project from the Ministry of Education, Culture, Sports, Science and Technology, Japan. C.N.K. is grateful for the support of a Grant-in-Aid for Specially Promoted Research (no. 16750126) from the Ministry of Education, Science, Sports and Culture of Japan, and the Association for the Progress of New Chemistry.

Supporting Information

The online version of this article contains additional supplementary material.

Please visit DOI:10.1016/j.jcat.2005.02.007.

References

[1] Z.V. Gryaznova, E.V. Kolodieva, V.P. Paranosenkov, G.V. Tsitsishvili, A.Yu. Krupennikova, Neftekhimiya 13 (1973) 374.
[2] B.F.G. Johnson, Top. Catal. 24 (2003) 147.
[3] J.S. Hjortkjaer, S. Michael, P. Simonsen, J. Mol. Catal. 6 (1979) 405.
[4] E.W. Thornton, H. Knoezinger, B. Tesche, J.J. Rafalko, B.C. Gates, J. Catal. 62 (1980) 117.
[5] M.D. Ward, J. Schwartz, J. Mol. Catal. 11 (1981) 397.
[6] J.P. Boitiaux, J. Cosyns, E. Robert, Appl. Catal. 35 (1987) 193.
[7] F. Sanchez, M. Iglesias, A. Corma, P.C. Del, J. Mol. Catal. 70 (1991) 369.
[8] A. Zsigmond, K. Bogar, F. Notheisz, J. Catal. 213 (2003) 103.
[9] A. Zsigmond, I. Balatoni, F. Notheisz, F. Joo, J. Catal. 227 (2004) 417.
[10] P.S. Skell, S.N. Ahmed, J. Catal. 125 (1990) 525.
[11] H.H. Wagner, H. Hausmann, W.F. Hoelderich, J. Catal. 203 (2001) 150.
[12] A.T. Bell, J. Mol. Catal. A 100 (1995) 1.
[13] M. Tada, T. Sasaki, Y. Iwasawa, J. Catal. 211 (2002) 496.
[14] M. Tada, T. Sasaki, T. Shido, Y. Iwasawa, Phys. Chem. Chem. Phys. 4 (2002) 5899.
[15] M. Tada, Y. Iwasawa, J. Mol. Catal. A 199 (2003) 115.
[16] F. Pinna, C. Candilera, G. Strukul, M. Bonivento, J. Org. Chem. 159 (1978) 91.
[17] J.M. Thomas, R. Raja, Chem. Rec. 1 (2001) 448.
[18] A. Frydman, D.G. Castner, C.T. Campbell, M. Schmal, J. Catal. 188 (1999) 1.
[19] T. Yokoyama, K. Yamazaki, N. Kosugi, H. Kuroda, M. Ichikawa, T. Fukushima, J. Chem. Soc., Chem. Commun. (1984) 962.
[20] M. Ichikawa, Polyhedron 7 (1988) 2351.
[21] A. Choplin, L. Huang, A. Theolier, P. Gallezot, J.M. Basset, U. Siriwardane, S.G. Shore, R. Mathieu, J. Am. Chem. Soc. 108 (1986) 4224.
[22] J.R. Anderson, D.E. Mainwaring, J. Catal. 35 (1974) 162.
[23] L. Tebassi, A. Sayari, A. Ghorbel, M. Dufaux, C. Naccache, J. Mol. Catal. 25 (1984) 397.
[24] Y. Huang, W.M.H. Sachtler, J. Catal. 188 (1999) 215.
[25] G.D. Angel, B. Coq, F. Figueras, J. Catal. 95 (1985) 167.
[26] J.R. Budge, B.F. Lucke, B.C. Gates, J. Toran, J. Catal. 91 (1985) 272.
[27] V. Schunemann, H. Trevino, G.D. Lei, D.C. Tomczak, W.M.H. Sachtler, K. Fogash, J.A. Dumesic, J. Catal. 153 (1995) 144.
[28] S. Irusta, L.M. Cornaglia, E.A. Lombardo, J. Catal. 210 (2002) 263.
[29] K.I. Choi, A.M. Vannice, J. Catal. 131 (1991) 22.
[30] K.I. Choi, A.M. Vannice, J. Catal. 131 (1991) 36.
[31] K. Nakano, K. Kusunoki, Chem. Eng. Commun. 34 (1985) 99.
[32] R.J. Pellet, J. Catal. 177 (1998) 40.
[33] A. Zhang, I. Nakamura, K. Fujimoto, J. Catal. 168 (1997) 328.
[34] E. Baumgarten, R. Krupp, React. Kinet. Catal. Lett. 70 (2000) 27.
[35] M. Ojeda, M.L. Granados, S. Rojas, P. Terreros, J.L.G. Fierro, J. Catal. 202 (2003) 179.
[36] M. Fujita, Y.J. Kwon, S. Washizu, K. Ogura, J. Am. Chem. Soc. 116 (1994) 1151.
[37] O.M. Yaghi, G. Li, H. Li, Nature (London) 378 (1995) 703.
[38] W. Mori, F. Inoue, K. Yoshida, H. Nakayama, S. Takamizawa, M. Kishita, Chem. Lett. (1997) 1219.
[39] V.A. Russell, C.C. Evans, W. Li, D. Michael, Science (Washington, D.C.) 276 (1997) 575.
[40] M. Kondo, T. Yoshitomi, K. Seki, H. Matsuzaka, S. Kitagawa, Angew. Chem. Int. Ed. Engl. 36 (1997) 1725.
[41] S. Kitagawa, M. Kondo, Bull. Chem. Soc. Jpn. 71 (1998) 1739.
[42] A. Nakamura, N. Ueyama, K. Yamaguchi, Organometallic Conjugation, Kodansha Springer, Tokyo, 2002, p. 179.
[43] W. Mori, S. Takamizawa, C.N. Kato, T. Ohmura, T. Sato, Micropor. Mesopor. Mater. 73 (2004) 31.
[44] Feinstein-Jaffe, A. Efraty, J. Mol. Catal. 40 (1987) 1.
[45] S. Naito, T. Tanibe, E. Saito, T. Miyao, W. Mori, Chem. Lett. (2001) 1178.
[46] T. Sato, W. Mori, C.N. Kato, T. Ohmura, T. Sato, K. Yokoyama, S. Takamizawa, S. Naito, Chem. Lett. 32 (2003) 854.
[47] A.D. Adler, F.R. Longo, F. Kampas, J. Kim, J. Inorg. Nucl. Chem. 32 (1970) 2443.
[48] R.F. Pasternak, L. Francesconi, D. Raff, E. Spiro, Inorg. Chem. 12 (1973) 2606.
[49] K. Nakamoto, Infrared and Raman Spectra of Inorganic and Coordination Compounds, Wiley, New York, 1986, p. 237.
[50] G.B. Deacon, R.J. Phillips, Coord. Chem. Rev. 33 (1980) 227.
[51] B. Bleaney, K.D. Bowers, Proc. R. Soc. London, Ser. A 214 (1952) 451.
[52] F.A. Cotton, R.A. Walton, Multiple Bonds between Metal Atoms, second ed., Clarendon, Oxford, NY, 1993, p. 431.
[53] E.A. Boundreaux, L.N. Mulay, Theory and Applications of Molecular Paramagnetism, Wiley, New York, 1993.
[54] G.M. Badger, R.A. Jones, R.L. Laslett, Aust. J. Chem. 17 (1964) 1028.
[55] R.L. Burwell Jr., Langmuir 2 (1986) 2.
[56] J.P. Boitiaux, J. Cosyns, E. Robert, Appl. Catal. 32 (1987) 145.
[57] J.A. Osborn, F.H. Jardine, J.F. Young, G. Wilkinson, J. Chem. Soc. A (1966) 1711.
[58] F.H. Jardine, J.A. Osborn, G. Wilkinson, J. Chem. Soc. A (1967) 1574.
[59] J. Halpern, Inorg. Chem. Acta 89 (1984) L53.
[60] Y. Ohtani, A. Yamagishi, M. Fujimoto, Bull. Chem. Soc. Jpn. 52 (1979) 69.
[61] L.F. Vieira, P.V. Cabral, P. Almeida, A.S. Oliveira, Macromolecules 31 (1998) 3936.
[62] S. Brunauer, L.S. Deming, W.E. Deming, E. Teller, J. Am. Chem. Soc. 62 (1940) 1723.
[63] G. Horvath, K. Kawazoe, J. Chem. Eng. Jap. 16 (1983) 470.
[64] D.W. Thomas, A.E. Martell, Org. Biol. Chem. 5 (1959) 5111.
[65] M. Umemiya, K. Sugiura, H. Miyasaka, T. Ishii, M. Yamashita, Bull. Chem. Soc. Jpn. 76 (2003) 2123.

Further reading

[66] C.N. Kato, M. Hasegawa, T. Sato, A. Yoshizawa, T. Inoue, W. Mori, J. Catal. 230 (2005) 226.
[67] J.A. Real, E. Andres, M.C. Munoz, M. Julve, T. Granier, A. Bousseksou, F. Varret, Science 268 (1995) 265.